

Inverse Design of Mechanical Metamaterials with Target Nonlinear Response via a Neural Accelerated Evolution Strategy

Bolei Deng,* Ahmad Zareei, Xiaoxiao Ding, James C. Weaver, Chris H. Rycroft, and Katia Bertoldi*

Materials with target nonlinear mechanical response can support the design of innovative soft robots, wearable devices, footwear, and energy-absorbing systems, yet it is challenging to realize them. Here, mechanical metamaterials based on hinged quadrilaterals are used as a platform to realize target nonlinear mechanical responses. It is first shown that by changing the shape of the quadrilaterals, the amount of internal rotations induced by the applied compression can be tuned, and a wide range of mechanical responses is achieved. Next, a neural network is introduced that provides a computationally inexpensive relationship between the parameters describing the geometry and the corresponding stress–strain response. Finally, it is shown that by combining the neural network with an evolution strategy, one can efficiently identify geometries resulting in a wide range of target nonlinear mechanical responses and design optimized energy-absorbing systems, soft robots, and morphing structures.

scaffolds should be designed to match the nonlinear response of the surrounding native tissue.^[1] Further, wearable and flexible electronics must accommodate the large deformations of soft biological tissues and reduce the stresses induced on the skin by their presence.^[2] Finally, it has been shown that reusable, rate-independent and self-recoverable energy-absorbing materials can be realized by engineering structures that display nonlinear responses characterized by sudden snapping-induced load drops.^[3,4]

Mechanical metamaterials have recently emerged as an effective platform to engineer systems with mechanical behaviors that are governed by geometry rather than composition.^[5–8] While initial efforts have focused on the design of metamaterials with negative properties in the

1. Introduction

From wearable devices and energy-absorbing systems to scaffolds and soft robots, many applications would benefit from the inverse design of materials with a target nonlinear mechanical response. For example, to enhance tissue regeneration,

linear regime,^[9–12] more recently it has been shown that highly nonlinear responses (often accompanied by large internal rotations) can be triggered by introducing into the architectures slender elements that are prone to elastic instabilities.^[5,13] These nonlinear behaviors not only display very rich physics but can also be exploited to enable advanced functionalities, such as shape morphing,^[14,15] energy absorption^[3,16–18] and programmability.^[19–21] Although it is well known that such functionalities can be tuned by altering the underlying geometry, the identification of architectures that result in a target nonlinear response is a non-trivial task.

Robust and efficient algorithms have been established to guide the design of structures with target response in the linear regime. These include gradient based methods such as shape^[22] and topology^[23] optimization, as well as machine learning algorithms.^[24–27] However, such approaches cannot be directly applied to the inverse design of nonlinear mechanical metamaterials. This is because the energy landscapes of the nonlinear systems typically display multiple minima separated by large energy barriers and, therefore, are very challenging to navigate. To efficiently explore such energy landscapes, metaheuristic algorithms such as evolution strategies,^[28–30] genetic algorithms^[31] and particle swarm optimization,^[32] have been successfully used. Further, since these algorithms require solving many times the forward problem, recent efforts have focused on reducing their computational cost by coupling them

B. Deng, A. Zareei, X. Ding, J. C. Weaver, C. H. Rycroft, K. Bertoldi
School of Engineering and Applied Sciences
Harvard University
Cambridge, MA 02138, USA
E-mail: boleideng@g.harvard.edu; bertoldi@seas.harvard.edu

B. Deng
Computer Science and Artificial Intelligence Laboratory
Massachusetts Institute of Technology
Cambridge, MA 02139, USA

B. Deng
Department of Mechanical Engineering
Massachusetts Institute of Technology
Cambridge, MA 02139, USA

C. H. Rycroft
Computational Research Division
Lawrence Berkeley Laboratory
Berkeley, CA 94720, USA

 The ORCID identification number(s) for the author(s) of this article can be found under <https://doi.org/10.1002/adma.202206238>.

DOI: 10.1002/adma.202206238

with machine learning models trained to solve the forward problem.^[33–38]

Here, we present a framework to design mechanical metamaterials with target nonlinear response. Our starting point is a metamaterial based on hinged rotating squares (see Figure 1a), which has recently attracted significant interest as it displays effective negative Poisson's ratio^[39–41] and supports the propagation of solitary pulses.^[42–44] We first show that changes in the shape of the quadrilateral units lead to a wide range of mechanical responses and identify the key ingredients governing such behaviors. Then, we use neural networks to accurately learn the relationship between the geometry of the metamaterials and their nonlinear mechanical response. Finally, we combine neural networks with an evolution strategy to efficiently identify geometries that exhibit target nonlinear stress–strain behaviors. The proposed neural accelerated evolution strategy holds potential for a range of applications that benefit from systems with a target nonlinear mechanical behavior, as demonstrated by the design of energy absorbing systems, soft robots and morphing structures.

2. Our Physical Platform

We start by testing under uniaxial compression two elastomeric metamaterials comprising a 10×8 array of hinged quadrilateral units flanked by two horizontal strips of solid material (Figure 1a). Both structures are realized by repeating a unit cell that consists of 2×2 units connected at their vertices by thin beam-like ligaments with width and length of 1 mm. The unit cell of one sample comprises four identical squares with center-to-center distance $a = 10$ mm, while that of the other consists of four different irregular quadrilaterals obtained by randomly perturbing the position of the squares vertices (while maintaining a unit cell size of $2a$ in both horizontal and vertical directions—Figure 1a and Sections S1 and S2, Supporting Information). In Figure 1b we show snapshots of the two structures at an applied compressive strain $\epsilon = -0.1$, while in Figure 1c we report the stress–strain curves recorded during our tests. We find that, although in both samples the deformation localizes at the beam-like hinges (which are identical in the two samples), their mechanical responses are remarkably different. In the sample with square units the buckling (and the subsequent bending) of the beam-like ligaments triggered at a critical compressive strain $\epsilon \approx -0.02$ makes all squares to alternatively rotate in clockwise and counter-clockwise direction.^[39,45,46] The shrinking associated with such collective rotational motion accommodates most of the additional applied strain and therefore limits the amount of compression in the vertical ligaments, ultimately leading to a stress plateau. By contrast, geometric frustration prevents rotation of the units in the sample comprising irregular quadrilaterals. It follows that for the sample comprising irregular quadrilaterals the applied deformation is almost entirely accommodated by the axial compression of the ligaments aligned along the vertical direction, resulting in a stiff and near-linear response.

The results of Figure 1 show that the shape of the quadrilaterals has a profound effect on the nonlinear mechanical response of the resulting metamaterial (see also Movie S1,

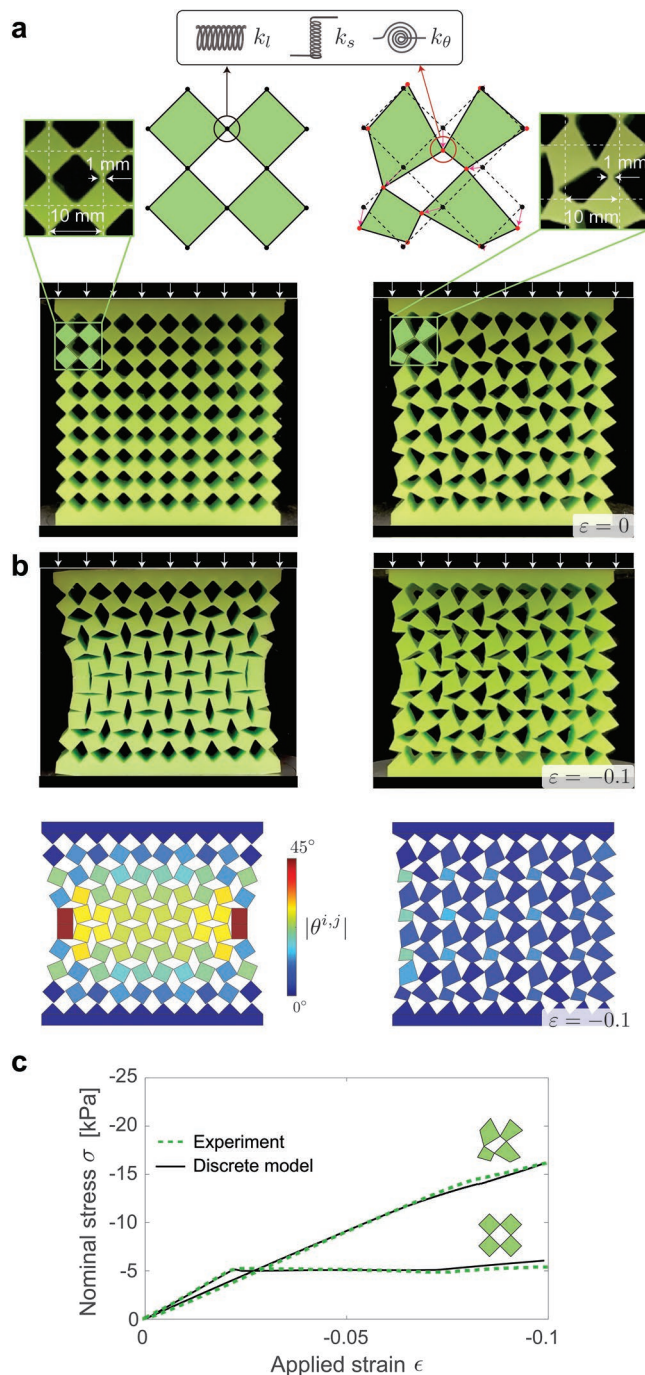


Figure 1. a) Top row: Unit cells of two structures comprising 2×2 quadrilateral units connected at their vertices by thin beam-like ligaments. The ligaments can be modeled using a combination of three linear springs with stiffness k_l , k_s , and k_θ . Bottom row: Pictures of the corresponding samples in the initial undeformed configuration. b) Top row: Pictures of the samples under $\epsilon = -0.1$ compression strain. Bottom row: Numerical snapshots of the samples under $\epsilon = -0.1$ compression strain. The color here indicates the local rotation of the quadrilaterals. c) Stress–strain response of the samples as measured in experiments (green dashed lines) and predicted by the discrete model (black lines).

Supporting Information). To systematically explore such effect, we make use of numerical simulations. In particular, since

our experiments indicate that under uniaxial compression the quadrilateral units remain rigid and the deformation localizes at the hinges, the nonlinear behavior of our structures can be described using a discrete model comprising rigid units connected at their vertices by a combination of three springs^[45,46] (see Figure 1a): (i) a linear spring with stiffness $k_1 = 0.47 \text{ N mm}^{-1}$ to capture the longitudinal response of the hinges; (ii) a linear spring with stiffness $k_s = 0.16 \text{ N mm}^{-1}$ to model their shearing; and (iii) a nonlinear hardening rotational spring that exert a torque $M = k_\theta \Delta\theta + \gamma \Delta\theta^3$ (where $\Delta\theta$ is the relative rotation between the connected quadrilaterals, $k_\theta = 0.088 \text{ N mm}$ and $\gamma = -0.2$) to capture their bending (see Section S3, Supporting Information). By imposing force equilibrium at each unit, we derive a system of coupled nonlinear equations that we numerically solve to obtain the response of the structure. Note that in this study we consider metamaterials with out-of-plane thickness large enough to prevent out-of-plane deformation and, therefore, limit the analyses to in-plane deformation. To test the relevance of our discrete model, we first compare its predictions to the experimental results reported in Figure 1 (see also Movie S1, Supporting Information). We find a very good agreement between our experimental and numerical results both in term of stress–strain curves and deformation field, confirming the validity of our model.

Next, we create 7500 different unit cells by randomly choosing the position of the quadrilateral vertices while preserving periodicity (see Figure 2a and Section S4, Supporting Information) and use our discrete model to simulate the mechanical response of the resulting metamaterials under uniaxial compression. In Figure 2b we report the numerically predicted stress–strain curves for all generated architectures. We find that a variety of nonlinear mechanical responses emerge. These include near-linear behaviors with a wide range of tangent moduli (see curves (i) and (ii) in Figure 2b for the upper and lower limits) as well as highly nonlinear behaviors that exhibit strain-softening and sudden load drops (see curves (iii) and (iv) in Figure 2b for representative examples). Further, our numerical results indicate that such different responses are accompanied by distinct deformation modes (see also Movie S2, Supporting Information). Focusing on the four architectures whose response is highlighted in Figure 2b, we find that at $\varepsilon = -0.1$ the rotations of the units are relatively small for the two structures that display near-linear responses and much larger for the two exhibiting nonlinear behaviors (see Figure 2c (top) and Movie S2, Supporting Information). Importantly, the connection between the internal rotations and nonlinearity is not limited to these four architectures. As shown in Figure 2d, for all 7500 metamaterials there is a correlation between the

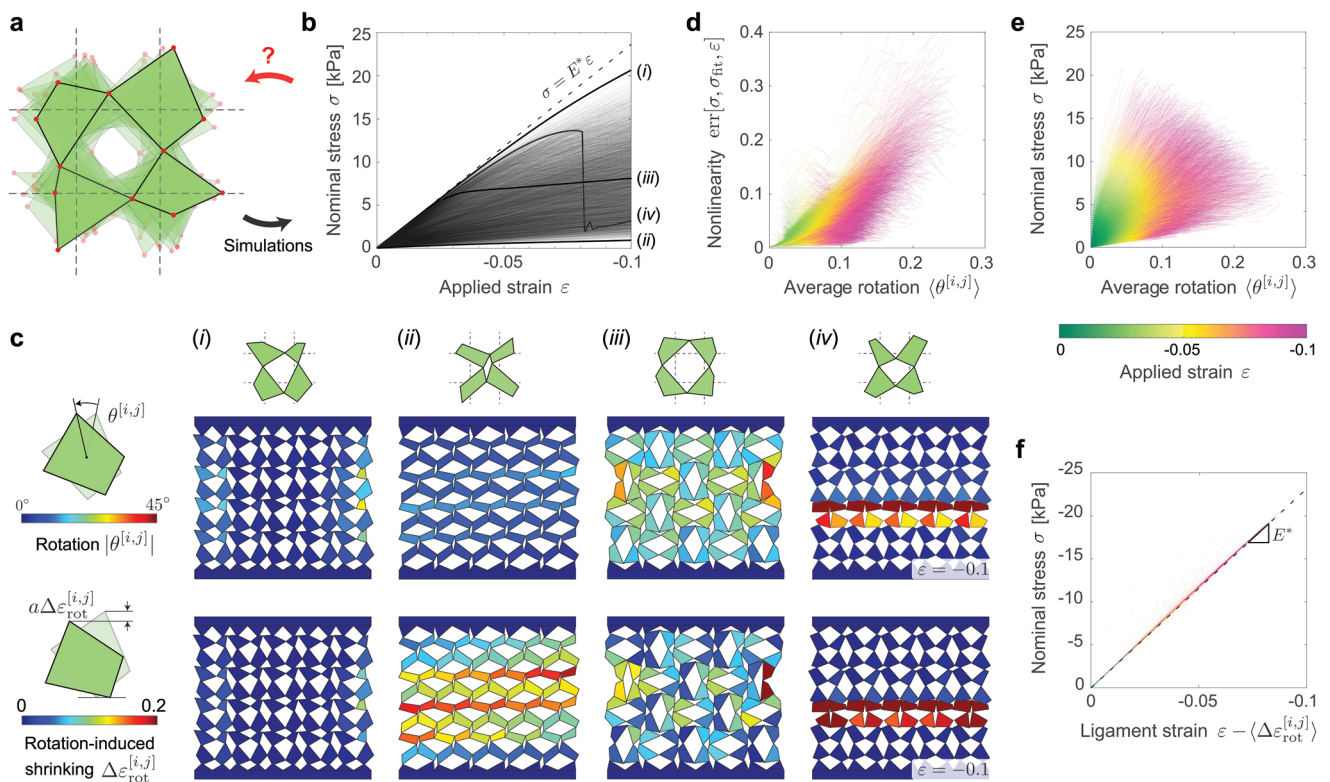


Figure 2. a) Unit cells generated by randomly perturbing the position of the quadrilaterals vertices, while preserving periodicity. b) Stress–strain curves predicted by the discrete model for 7500 different metamaterials realized by tessellating different unit cells. Four representative stress–strain curves are highlighted. These include (i)–(ii) near-linear behaviors with a wide range of stiffness; (iii) stress–strain curves with an initial linear regime followed by a plateau; and (iv) stress–strain curves displaying sudden drops in force. The upper bound $\sigma = E^* \varepsilon$ is shown as a dashed black line. c) Numerical snapshots of the structures highlighted in (b) at $\varepsilon = -0.1$. The color in the top row indicates the rotation of the quadrilaterals, while the color in the bottom row indicates the rotation-induced shrinking. d) Average nonlinearity ($\text{err}[\sigma, \sigma_{\text{fit}}, \varepsilon]$) versus average rotation ($\langle \theta^{[i,j]} \rangle$) for all 7500 metamaterials at different level of applied strain. e) Nominal stress (σ) versus average rotation ($\langle \theta^{[i,j]} \rangle$) for all 7500 metamaterials at different levels of applied strain. f) Nominal stress (σ) versus strain accommodated by a column of vertical ligaments ($\varepsilon - \langle \Delta \varepsilon_{\text{rot}}^{[i,j]} \rangle$) for all 7500 metamaterials at different levels of applied strain.

average rotation of the units, $\langle \theta^{[i,j]} \rangle$ (where $\theta^{[i,j]}$ denotes the rotation of the $[i,j]$ -th unit), and the amount of nonlinearity displayed by the corresponding stress–strain curve. Note that the latter is quantified using the normalized root mean squared error between the stress–strain curve and its best linear fit, $\text{err}[\sigma, \sigma_{\text{fit}}, \epsilon]$, where $\sigma_{\text{fit}} = E\epsilon$ represents the best linear fit to the curve and

$$\text{err}[f, g, \epsilon] = \sqrt{\frac{\int_0^\epsilon (f(\epsilon') - g(\epsilon'))^2 d\epsilon'}{\int_0^\epsilon f(\epsilon')^2 d\epsilon'}} \quad (1)$$

with the integrals being evaluated numerically. Near-linear responses (for which $\text{err}[\sigma, \sigma_{\text{fit}}, \epsilon] \rightarrow 0$) are accompanied by small rotations of the units, whereas large internal rotations lead to highly nonlinear behaviors characterized by large values of $\text{err}[\sigma, \sigma_{\text{fit}}, \epsilon]$.

Differently, we find that there is no correlation between $\langle \theta^{[i,j]} \rangle$ and the recorded nominal stress, σ (see Figure 2e). This is because small internal rotations can be amplified by the geometry of the quadrilaterals and result in large amount of shrinking along the vertical direction (see Figure 2c-ii). Such rotation-induced shrinking reduces the level of axial compression in the ligaments and therefore is expected to affect the measured nominal stress. To quantify this effect, we define the rotation-induced shrinking along the vertical direction for the $[i,j]$ -th unit as

$$\Delta \epsilon_{\text{rot}}^{[i,j]}(\epsilon) = \frac{(\gamma_{\text{top}}^{[i,j]}(\epsilon) - \gamma_{\text{b}}^{[i,j]}(\epsilon)) - (\gamma_{\text{top}}^{[i,j]}(0) - \gamma_{\text{b}}^{[i,j]}(0))}{a} \quad (2)$$

where $\gamma_{\text{top}}^{[i,j]}(\epsilon)$ and $\gamma_{\text{b}}^{[i,j]}(\epsilon)$ denote the y -coordinate of the top and bottom vertex of the $[i,j]$ -th quadrilateral at ϵ . The numerical snapshots reported in Figure 2c (bottom) confirm that $\Delta \epsilon_{\text{rot}}^{[i,j]}$ can be large even in structures that display small internal rotations (see Figure 2c-ii). As a matter of fact, there is a strong correlation between σ and the average rotation-induced shrinking, $\langle \Delta \epsilon_{\text{rot}}^{[i,j]} \rangle$. More specifically, since the compressive strain accommodated by a column of vertical ligaments is given by $\epsilon - \langle \Delta \epsilon_{\text{rot}}^{[i,j]} \rangle$, we find that for all considered metamaterials

$$\sigma \approx E^* (\epsilon - \langle \Delta \epsilon_{\text{rot}}^{[i,j]} \rangle) \quad (3)$$

where E^* is the effective Young's modulus of the metamaterial in the absence of rotations (see Figure 2f). Note that $E^* = 10k_1/(9b)$, where b denotes the out-of-plane thickness of the metamaterial, since our structure comprises 10 columns of vertical ligaments with longitudinal stiffness k_1 , each consisting of 9 ligaments arranged in series. It follows from Equation (3) that the stiffest response for the considered class of metamaterials can be achieved in the absence of rotations (i.e., for $\langle \Delta \epsilon_{\text{rot}}^{[i,j]} \rangle = 0$) and is given by $\sigma = E^* \epsilon$ (see dashed line in Figure 2b). As such, our results indicate that by tuning the amount of rotation-induced shrinking upon compression we can successfully manipulate the stress–strain curves of the considered class of metamaterials. Importantly, this tuning can be accomplished by varying the geometry of the quadrilateral units.

3. Neural Networks

While in Figure 2 we focus on the mechanical response of 7500 architectures, our numerically generated stress–strain curves enable prediction of the behavior of metamaterials realized out of arbitrary unit cells. This is because such data can serve as offline training of a machine-learning (ML) model that provides a computationally inexpensive relationship between the parameters describing the unit cell geometry and the corresponding stress–strain response. To this end, we represent the p -th unit cell in our database as a 16-dimensional vector $\mathbf{X}_p = [\mu_p^1, \nu_p^1, \dots, \mu_p^8, \nu_p^8]^\top$, where μ_p^α and ν_p^α represent the perturbations in horizontal and vertical directions applied to its α -th independent vertex for the p -th unit cell (see Section S1, Supporting Information) and the corresponding stress–strain curve as a 100-dimensional vector $\sigma_p = [\sigma_p(0), \dots, \sigma_p(-0.1)]^\top$, which contains the stress values at 100 equally spaced strain points. Note that, although we simulated 7500 metamaterials, our dataset contains a total of $N = 30\,000$ datapoints, since the response of all designs remains unaltered when they are reflected over the x -axis, the y -axis and in the origin (see Figure 3a). Out of the expanded dataset, we randomly choose $N_{\text{tr}} = 0.8N$ datapoints for training and the remaining $N_{\text{test}} = 0.2N$ for testing.

To facilitate training of the ML model, we reduce the dimensionality of the stress vectors by using principal component analysis (PCA).^[47] In particular, we describe the stress–strain curve of the p -th design via its first 10 principal components, $\sigma_p^{\text{PC}_{10}}$. Note that this leads to an average reconstruction error of $\frac{1}{N_{\text{tr}}} \sum_{p=1}^{N_{\text{tr}}} \text{err}[\sigma_p, \sigma_p^{\text{R}}, -0.1] = 0.3\%$, where σ_p denotes the true stress vector and σ_p^{R} the reconstructed one from the first 10 principal components (Section S5, Supporting Information).

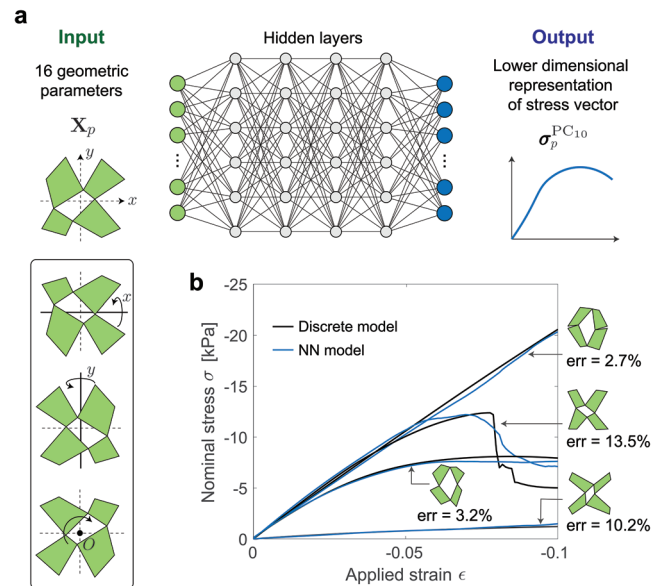


Figure 3. a) Our NN architecture has four hidden layers, each comprising 200 neurons. A 16-dimensional vector \mathbf{X}_p is fed to the NN that is trained to predict the lower-dimensional representation of the corresponding stress vector $\sigma_p^{\text{PC}_{10}}$. b) Comparison between the stress–strain curves predicted by our discrete (black solid lines) and NN (dashed blue lines) models for four geometries that are part of the test dataset.

To predict the lower dimensional representation of the stress vector, $\sigma_p^{\text{PC}_{10}}$, for a given geometry, \mathbf{X}_p , we use a neural network (NN) architecture with four hidden layers, each comprising 200 neurons (see Figure 3a and Section S6, Supporting Information). We train the NN by selecting the neuron weights and biases that minimize

$$\mathcal{L} = \sum_{p=1}^{N_t} \sum_{s=1}^{10} \beta_s (\mathcal{F}_s(\mathbf{X}_p) - \sigma_{p,s}^{\text{PC}_{10}})^2 \quad (4)$$

where $\sigma_{p,s}^{\text{PC}_{10}}$ is the s -th component of $\sigma_p^{\text{PC}_{10}}$, $\mathcal{F}(\mathbf{X}_p) = [\mathcal{F}_1(\mathbf{X}_p), \dots, \mathcal{F}_{10}(\mathbf{X}_p)]^\top$ denote the corresponding NN predictions and β_s is the variance explained in the s -th principal component (Section S5, Supporting Information). Finally, to evaluate the accuracy of our trained NN, we reconstruct the stress-strain response from $\mathcal{F}(\mathbf{X}_p)$ and calculate the average relative

error on the test dataset as $\frac{1}{N_{\text{test}}} \sum_{p=1}^{N_{\text{test}}} \text{err}[\sigma_p, \sigma_p^{\text{NN}}, -0.1]$, where σ_p^{NN} is

the stress vector reconstructed from $\mathcal{F}(\mathbf{X}_p)$. We find that the trained NN accurately predicts the stress-strain curves associated to unseen designs, with an average relative error of 4.8%. As examples, in Figure 3b we focus on four designs that are part of the test dataset and display distinct mechanical behaviors. The comparison between the stress-strain curves predicted by our discrete and NN models for these four geometries indicates that our trained NN can capture all behaviors that are representative of the considered class of mechanical metamaterials, with discrepancies that are more accentuated for the stress-strain curves displaying sharp drops in force. This is because such sharp drops are induced by the snapping of a few

unit cells (see numerical snapshot at $\varepsilon = -10$ in Figure 2c-iv)—a phenomenon that is known to be very sensitive to geometric perturbations^[48] and, therefore, difficult to predict.

4. Inverse Design

Our trained NN enables us to efficiently determine the mechanical response of arbitrary metamaterials. However, since the connection between the geometry of the unit cells and the mechanical response of the corresponding structure is not trivial, identification of metamaterials with target behavior requires an efficient inverse design strategy. Toward this end, as shown in Figure 4a, we couple our trained NN with an evolution strategy (ES)—a type of stochastic global optimization algorithm inspired by the biological theory of evolution.^[28] To test our approach, we focus on four distinct target behaviors (see Figure 4b)

$$\begin{aligned} \sigma_t^{(i)} &= E^* \varepsilon \\ \sigma_t^{(ii)} &= 0.8 \sigma_{\text{soft}} \\ \sigma_t^{(iii)} &= E^* (\varepsilon + 9\varepsilon^2) \\ \sigma_t^{(iv)} &= \begin{cases} 0.8E^* \varepsilon, & \text{if } \varepsilon > -0.07 \\ -0.025E^*, & \text{if } \varepsilon < -0.07 \end{cases} \end{aligned} \quad (5)$$

where σ_{soft} denotes the softest response within the dataset and "t" indicates "target". Note that $\sigma_t^{(i)}$ represents the stiffest possible response for the considered class of metamaterials (see Equation (3)), whereas $\sigma_t^{(ii)}$ describes a near-linear stress-strain curve that is 20% softer than the softest one within the dataset. Further, $\sigma_t^{(iii)}$ represents a smooth stress-strain curve

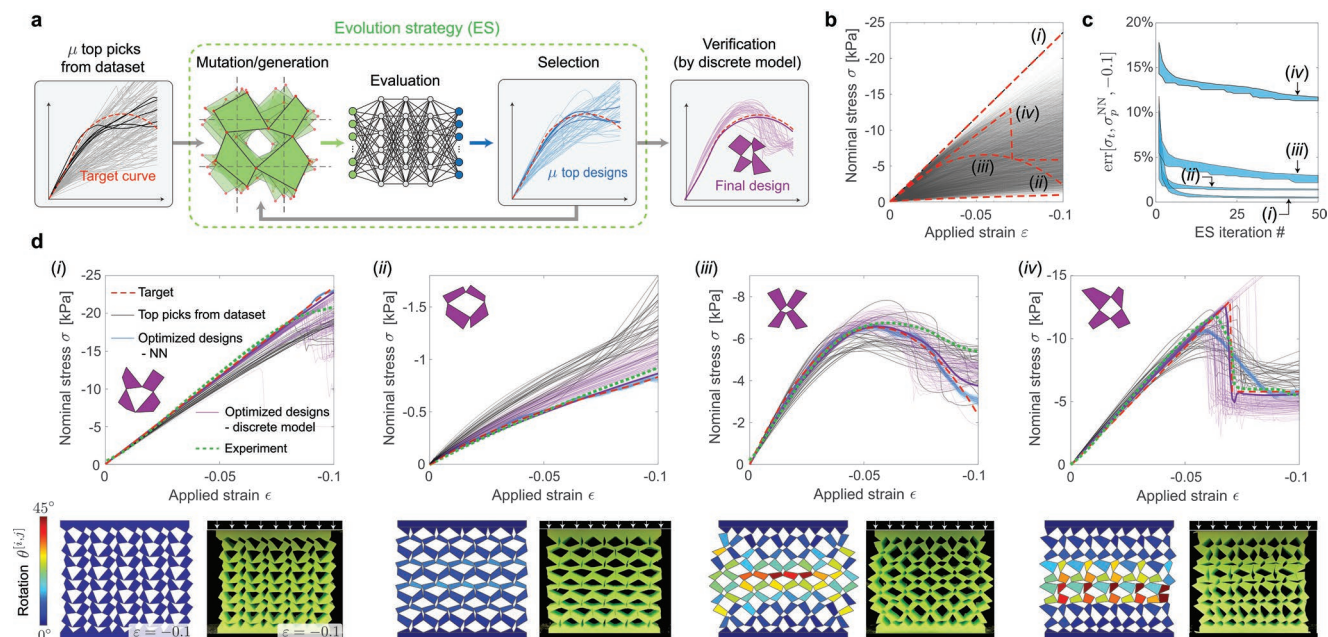


Figure 4. a) Schematic representing the proposed inverse design algorithm based on a neural accelerated evolution strategy. b) The four target stress-strain curves considered in this study. c) Evolution of $\max_p \text{err}[\sigma_p, \sigma_p^{\text{NN}}, -0.1]$ during ES iterations for the four considered targets. d) Target response (red dashed line), top picks from dataset (black lines) and stress-strain curves predicted by our trained NN (blue lines) and our discrete model (purple lines) for the optimized designs. The designs that minimize $\text{err}[\sigma_p, \sigma_p^{\text{DM}}, -0.1]$ are shown as inset. For each of these designs we also show numerical and experimental snapshots at $\varepsilon = -0.1$. The color in the numerical snapshots indicates the local rotation of the quadrilaterals.

that display a strain-induced stress drop more accentuated than those found in the dataset and $\sigma^{(iv)}$ is characterized by a sharp drop in stress at an unseen location. To identify geometries leading to these target behaviors, we start by selecting $\mu = 100$ stress–strain curves from our dataset that minimize $\text{err}[\sigma_t, \sigma_p, -0.1]$. As expected, no response in the dataset closely matches our four target behaviors (see black lines in Figure 4d)—with a minimum error between the top picks and the target ones equal to: (i) 11%, (ii) 25%, (iii) 13% and (iv) 12%. Next, in an attempt to reduce these errors, we generate $\lambda = 49$ new candidate geometries (the children) from each of the unit cells associated to these solutions (the parents) by randomly moving their eight independent vertices within boxes with edge of $0.1a$ centred around them. Further, to better explore the design space, we generate 5000 completely arbitrary unit cells that compete with the parents and children for consideration in the next iteration (see Figure S17, Supporting Information for a discussion on the benefits of adding these 5000 arbitrary unit cells). The parents, children, and arbitrary unit cells form a set of 10 000 geometries, whose stress–strain curves are determined using our trained NN. Out of this set, we then select the parents for the next iteration by choosing the $\mu = 100$ designs that minimize $\text{err}[\sigma_t, \sigma_p^{\text{NN}}, -0.1]$ and we continue this mutation/generation and selection process until there are $\mu = 100$ designs for which $\max_p(\text{err}[\sigma_t, \sigma_p^{\text{NN}}, -0.1]) < 1\%$, or 50 iterations are reached. It is important to note that the trained NN enables us to largely reduce the computation time required to identify the optimal designs, since it takes only 0.2 s for the NN to evaluate 10 000 designs (whereas it takes 23.2 days for the the discrete model to evaluate 10 000 designs).^[49] In Figure 4c we report the evolution of $\text{err}[\sigma_t, \sigma_p^{\text{NN}}, -0.1]$ for the best performing $\mu = 100$ designs over the course of each iteration, whereas in Figure 4d we show as blue lines the stress–stress curves predicted by our trained NN for the optimized $\mu = 100$ designs identified by the ES. We find that the error between the optimal curves and the target ones is largely reduced for the considered first three targets. Differently, the reduction in error is less significant for the fourth target response, as 10 principal components are not enough to capture a stress–strain curve with a sharp drop in load (see blue lines in Figure 4d-iv). Although such error could be reduced by considering a larger number of principal components to represent the stress–strain curve, it is important to point out that this would not necessarily translate to a better solution. This is because the trained NN introduces an error in the estimation of their mechanical responses, which becomes more accentuated for designs that are very different from those included in the training dataset. As a matter of fact, when we use the discrete model to simulate the final $\mu = 100$ designs identified by ES, we find an average error $\frac{1}{\mu} \sum_p \text{err}[\sigma_p, \sigma_p^{\text{DM}}, -0.1] = 15\%$ on these optimized designs (see purple lines in Figure 4d)—much higher than that obtained on the test set (4.8%). However, despite the error introduced by the NN, the $\mu = 100$ optimized designs identified by ES display stress–strain curves that are on average much closer to the target curves than the close matches from the dataset (black curves). More specifically, we find that the minimum error between σ_t and the stress–strain curve predicted by the discrete model for the μ optimized geometries, σ_p^{DM} , is reduced

to: (i) 1.9%, (ii) 4.7%, (iii) 6.6%, and (iv) 4.5% (the designs that best match the target curves are shown as thick purple curves in Figure 4d).

Next, we physically fabricate the optimized designs that closely match the target curves and report the experimentally recorded stress–strain curves (green dashed lines) as well as snapshots of the samples at $\varepsilon = -0.1$ in Figure 4d (see also Movie S3, Supporting Information). Despite the unavoidable imperfections introduced during fabrication and testing, the recorded stress–strain curves closely match the target ones. Focusing on the first target, we find that our optimization framework identifies a geometry that prevents internal rotations under compression and, as predicted by Equation (3), results in the stiffest possible response. As for the second target, the inversely designed metamaterial comprises highly tilted (almost flat) elongated quadrilaterals that maximize the rotation-induced shrinking and therefore lead to a very compliant response. Differently, the optimized geometry for the third target consists of elongated quadrilaterals that are almost aligned along the vertical direction. Upon compression these units gradually rotate (see Figure 4d-iii), so that the structure approaches the optimized geometry for the second target and, therefore, becomes much softer. Finally, the fourth optimized design comprises two rows of quadrilaterals that snap at the target strain, yielding a sudden load drop.

5. Conclusions

We have introduced a neural accelerated evolution strategy to identify mechanical metamaterials with target nonlinear response.

These optimized metamaterials provide opportunities for the design of a wide range of smart structures, including energy-absorbing systems and soft robots. To investigate the energy-absorbing performance upon impact of our inversely designed metamaterials, we conduct drop tests on the optimized structures reported in Figure 4. More specifically, we drop a circular acrylic disk (with mass $m_{\text{disk}} = 100$ g and diameter $d_{\text{disk}} = 100$ mm) onto their top surface from an height of 40 cm and measure the rebound height after the impact. As shown in Figure 5a and Figure S3, Supporting Information, we find that after the impact the disk bounces back to a height of 22.0, 15.3, 11.5 and 2.5 cm for the four considered structures, resulting in an absorption efficiency of 45%, 62%, 71% and 94%, respectively (see Section S2.C, Supporting Information for more details). The superior performance of the architecture optimized to match $\sigma^{(iv)}$ confirms that snapping provides a simple yet effective mechanism to realize reusable energy-absorbing materials^[50] and further indicate that our numerical strategy can be harnessed to optimize their absorption efficiency.

Additionally, while in this study we have focused on target nonlinear stress–strain responses, our neural accelerated evolution strategy can be readily applied to other nonlinear properties, providing a platform to facilitate the design of soft robots and actuators. For example, it has been shown that a soft robot capable of moving through a channel when actuated with a single input can be realized by combining two flexible structures with Poisson's ratio of equal magnitude but opposite

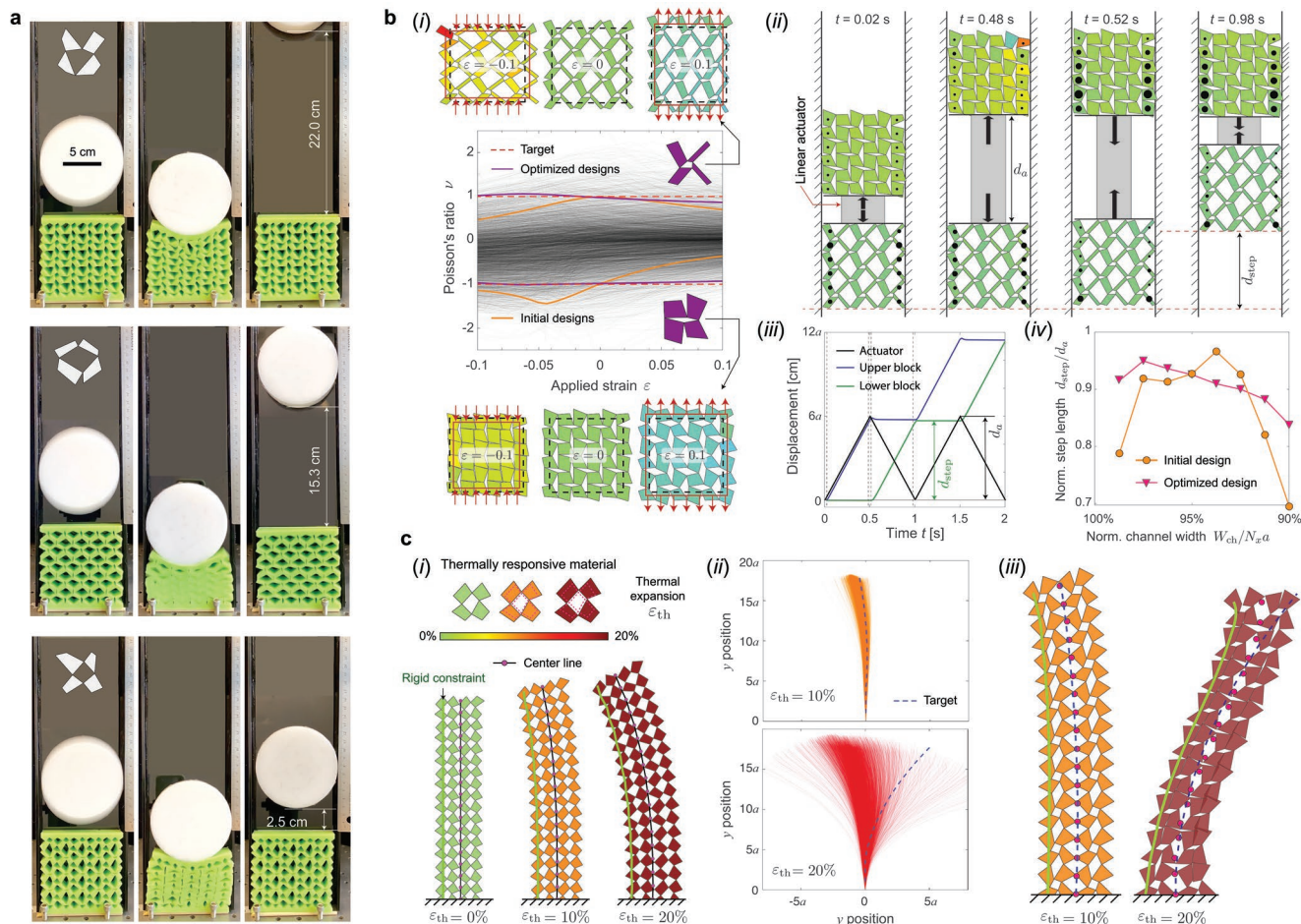


Figure 5. a) Energy absorption: Experimental images taken during the drop tests immediately before contact (left), at contact (center) and at the maximum height at which the disk bounces back after impact (right) for the metamaterial optimized to match $\sigma_i^{(i)}$ (top), $\sigma_i^{(ii)}$ (center) and $\sigma_i^{(iv)}$ (bottom). For these three structures we measure a contact time of 33, 75 and 96 ms and the height of the first bounce after the impact to be 22.0, 15.3, and 2.5 cm, resulting in an absorption efficiency $\eta = 45\%$, 62% , and 94% , respectively. b) Inverse design of soft robots that exploit auxetic behavior. (i) Evolution of the effective Poisson's ratio ν as a function of the applied strain ϵ predicted by the discrete model for 7500 different metamaterials realized by tessellating different unit cells. The neural accelerated evolution strategy is used to inverse design two architectures with constant Poisson's ratio $\nu(\epsilon) = \pm 1$ for $\epsilon \in [-0.1, 0.1]$. (ii) Numerical snapshots of the soft robot realized by connecting the two inversely designed metamaterials through a linear actuator moving into a channel with width $W_{ch} = 0.99N_x a$ at time $t = 0.02$ s, 0.48 s, 0.52 s, and 0.98 s. The color here indicates the local rotation of the quadrilaterals. (iii) Relative displacement imposed by the linear actuator (black line) and displacement of the center of mass of the lower (green line) and upper (blue line) blocks as a function of time. (iv) Evolution of the displacement recorded at the end of each cycle, d_{step} (normalized by the actuator stroke d_a) as a function of $W_{ch}/(N_x a)$ for the initial design (yellow markers) and the optimized design (magenta markers). c) Inverse design of structures capable of target deformations upon heating. (i) We consider a structure comprising 8×2 unit cells and assume that each quadrilateral unit expands uniformly under an increasing temperature. To trigger bending, we fix the center-to-center distance of the units on the left boundary. (ii) The distribution of the center lines of 7500 different unit cell designs at $\epsilon_{th} = 0.1$ (top) and 0.2 (bottom). The blue dashed lines represent the target curves at different thermal strains. (iii) The inverse designed metamaterial is able to closely match the target center lines at $\epsilon_{th} = 0.1$ and 0.2 .

sign.^[51] However, since mechanical metamaterials typically exhibit varying Poisson's ratio in the nonlinear regime,^[52,53] the efficiency of such robots largely varies with the width of the channel (Figure 5b(iv)). To overcome this limitation, we inverse design two architectures with constant Poisson's ratio $\nu = \pm 1$ over a large range of deformations (i.e., for $-0.1 < \epsilon < 0.1$) via our neural accelerated evolution strategy. As shown in Figure 5b(iv), the identified optimal structures lead to a soft robot with inch-worm locomotion that is less affected by the width of the channel (see Section S8.A, Supporting Information for more details). Finally, our neural accelerated evolution strategy can be exploited to identify structures capable of target deformation

upon application of an external stimulus, opening avenues for the inverse design of metamaterial-based soft actuators. To demonstrate this point, we consider a structure comprising 8×2 unit cells and assume that each quadrilateral unit expands uniformly under an increasing temperature (Figure 5c(i)). When the center-to-center distance of the units on the left boundary is fixed, the structures built out of the 7500 unit cells considered in this study bend into a variety of configurations upon heating (Figure 5c(ii)). Remarkably, we find that also in this case the neural network is able to learn the relation between the unit cell design and the deformed configuration and can be combined with evolution strategy to efficiently inverse design

architectures capable of supporting multiple target deformation modes (see Figure 5c(iii)) for a structure that bends toward the left for a thermal expansion $\epsilon_{th} = 10\%$ and toward the right for $\epsilon_{th} = 20\%$ —see Section S8.B, Supporting Information for more details).

To conclude, since the response of the inversely designed metamaterials is scale- and material-independent, we envisage that our strategy could be applied to the design of the next generation of flexible structures with target nonlinear behavior, ranging from large-scale energy-absorbing systems to small-scale robotic components.

Supporting Information

Supporting Information is available from the Wiley Online Library or from the author.

Acknowledgements

This research was supported by the NSF grants DMR-2011754, DMREF-1922321, OAC-2118201. K.B. also acknowledges support from the Simons Collaboration on Extreme Wave Phenomena Based on Symmetries.

Conflict of Interest

The authors declare no conflict of interest.

Author Contributions

B.D. and A.Z. contributed equally to this work. B.D. and K.B. designed the research. B.D. designed and conducted experiments, coded the discrete model and designed the neural accelerated evolution strategy. A.Z. fabricated samples, conducted experiments and analyzed the performance of neural networks. X.D. contributed to the original research idea, helped with experiments, and conducted preliminary neural network training. J.W. printed the molds for samples fabrication. B.D., A.Z. and K.B. wrote the manuscript. K.B. and C.R. supervised the research.

Data Availability Statement

The data that support the findings of this study are openly available in github at <https://github.com/boleideng94/metamaterials-inverse-design>.

Keywords

mechanical metamaterials, neural networks, nonlinear response, optimization

Received: July 9, 2022
Published online:

[1] B. Chan, K. Leong, *Eur. Spine J.* **2008**, *17*, 467.

[2] Y. Ma, X. Feng, J. A. Rogers, Y. Huang, Y. Zhang, *Lab Chip* **2017**, *17*, 1689.

- [3] S. Shan, S. H. Kang, J. R. Raney, P. Wang, L. Fang, F. Candido, J. A. Lewis, K. Bertoldi, *Adv. Mater.* **2015**, *27*, 4296.
- [4] Y. Chen, L. Jin, *Adv. Funct. Mater.* **2021**, 2102113.
- [5] K. Bertoldi, V. Vitelli, J. Christensen, M. Van Hecke, *Nat. Rev. Mater.* **2017**, *2*, 1.
- [6] M. Kadic, G. W. Milton, M. van Hecke, M. Wegener, *Nat. Rev. Phys.* **2019**, *1*, 198.
- [7] A. A. Zadpoor, *Mater. Horiz.* **2016**, *3*, 371.
- [8] J. Christensen, M. Kadic, O. Kraft, M. Wegener, *MRS Commun.* **2015**, *5*, 453.
- [9] Z. G. Nicolaou, A. E. Motter, *Nat. Mater.* **2012**, *11*, 608.
- [10] R. Lakes, *Science* **1987**, *235*, 1038.
- [11] R. Gatt, L. Mizzi, J. I. Azzopardi, K. M. Azzopardi, D. Attard, A. Casha, J. Briffa, J. N. Grima, *Sci. Rep.* **2015**, *5*, 8395.
- [12] M. Kadic, T. Bückmann, N. Stenger, M. Thiel, M. Wegener, *Appl. Phys. Lett.* **2012**, *100*, 191901.
- [13] P. M. Reis, *J. Appl. Mech.* **2015**, *82*, 111001.
- [14] L. Jin, A. E. Forte, B. Deng, A. Rafsanjani, K. Bertoldi, *Adv. Mater.* **2020**, *32*, 2001863.
- [15] J. W. Boley, W. M. van Rees, C. Lissandrello, M. N. Horenstein, R. L. Truby, A. Kotikian, J. A. Lewis, L. Mahadevan, *Proc. Natl. Acad. Sci. USA* **2019**, *116*, 20856.
- [16] C. M. Portela, B. W. Edwards, D. Veyssset, Y. Sun, K. A. Nelson, D. M. Kochmann, J. R. Greer, *Nat. Mater.* **2021**, *20*, 1491.
- [17] B. Haghpanah, L. Salari-Sharif, P. Pourrajab, J. Hopkins, L. Valdevit, *Adv. Mater.* **2016**, *28*, 7915.
- [18] D. Restrepo, N. D. Mankame, P. D. Zavattieri, *Ext. Mech. Lett.* **2015**, *4*, 52.
- [19] B. Florijn, C. Coulais, M. van Hecke, *Phys. Rev. Lett.* **2014**, *113*, 175503.
- [20] E. Medina, P. E. Farrell, K. Bertoldi, C. H. Rycroft, *Phys. Rev. B* **2020**, *101*, 064101.
- [21] T. Chen, M. Pauly, P. M. Reis, *Nature* **2021**, *589*, 386.
- [22] J. Sokolowski, J.-P. Zolésio, in *Introduction to Shape Optimization*, Springer, Berlin/Heidelberg, Germany **1992**, pp. 5–12.
- [23] O. Sigmund, K. Maute, *Struct. Multidiscip. Optim.* **2013**, *48*, 1031.
- [24] Y. Mao, Q. He, X. Zhao, *Sci. Adv.* **2020**, *6*, eaaz4169.
- [25] S. Kumar, S. Tan, L. Zheng, D. M. Kochmann, *npj Comput. Mater.* **2020**, *6*, 73.
- [26] G. X. Gu, C.-T. Chen, M. J. Buehler, *Ext. Mech. Lett.* **2018**, *18*, 19.
- [27] Z. Zhang, G. X. Gu, *Theor. Appl. Mech. Lett.* **2021**, 100220.
- [28] H.-G. Beyer, H.-P. Schwefel, *Nat. Comput.* **2002**, *1*, 3.
- [29] N. Hansen, A. Ostermeier, *Evol. Comput.* **2001**, *9*, 159.
- [30] N. Hansen, S. D. Müller, P. Koumoutsakos, *Evol. Comput.* **2003**, *11*, 1.
- [31] L. D. Davis, *Handbook of Genetic Algorithms*, Van Nostrand Reinhold, New York **1991**.
- [32] J. Kennedy, R. Eberhart, in *Proc. ICNN 95 - Int. Conf. on Neural Networks*, vol. 4, IEEE, Piscataway, NJ, USA **1995**, pp. 1942–1948.
- [33] Z. Yang, C.-H. Yu, M. J. Buehler, *Sci. Adv.* **2021**, *7*, eabd7416.
- [34] J. K. Wilt, C. Yang, G. X. Gu, *Adv. Eng. Mater.* **2020**, *22*, 1901266.
- [35] G. X. Gu, C.-T. Chen, D. J. Richmond, M. J. Buehler, *Mater. Horiz.* **2018**, *5*, 939.
- [36] S. Babaei, J. Shim, J. C. Weaver, E. R. Chen, N. Patel, K. Bertoldi, *Adv. Mater.* **2013**, *25*, 5044.
- [37] L. Wu, L. Liu, Y. Wang, Z. Zhai, H. Zhuang, D. Krishnaraju, Q. Wang, H. Jiang, *Ext. Mech. Lett.* **2020**, *36*, 100657.
- [38] S. Wu, C. M. Hamel, Q. Ze, F. Yang, H. J. Qi, R. Zhao, *Adv. Intell. Syst.* **2020**, *2*, 2000060.
- [39] K. Bertoldi, P. Reis, S. Willshaw, T. Mullin, *Adv. Mater.* **2010**, *22*, 361.
- [40] J. N. Grima, K. E. Evans, *J. Mater. Sci. Lett.* **2000**, *19*, 1563.
- [41] Y. Cho, J.-H. Shin, A. Costa, T. A. Kim, V. Kunin, J. Li, S. Y. Lee, S. Yang, H. N. Han, I.-S. Choi, et al., *Proc. Natl. Acad. Sci. USA* **2014**, *111*, 17390.

- [42] B. Deng, J. Raney, V. Tournat, K. Bertoldi, *Phys. Rev. Lett.* **2017**, *118*, 204102.
- [43] B. Deng, C. Mo, V. Tournat, K. Bertoldi, J. R. Raney, *Phys. Rev. Lett.* **2019**, *123*, 024101.
- [44] H. Yasuda, L. Korpas, J. Raney, *Phys. Rev. Appl.* **2020**, *13*, 054067.
- [45] C. Coulais, C. Kettenis, M. van Hecke, *Nat. Phys.* **2018**, *14*, 40.
- [46] B. Deng, S. Yu, A. E. Forte, V. Tournat, K. Bertoldi, *Proc. Natl. Acad. Sci. USA* **2020**, *117*, 31002.
- [47] I. T. Jolliffe, J. Cadima, *Philos. Trans. R. Soc., A* **2016**, *374*, 20150202.
- [48] A. Lee, F. López Jiménez, J. Marthelot, J. W. Hutchinson, P. M. Reis, *J. Appl. Mech.* **2016**, *83*, 11.
- [49] CPU used is a 9th Generation “Coffee Lake” 2.4 GHz Intel Core i9 processor i9-9980HK.
- [50] K. Fu, Z. Zhao, L. Jin, *Adv. Funct. Mater.* **2019**, *29*, 1901258.
- [51] A. G. Mark, S. Palagi, T. Qiu, P. Fischer, in *2016 IEEE Int. Conf. on Robotics and Automation (ICRA)*, IEEE, Piscataway, NJ, USA **2016**, pp. 4951–4956.
- [52] N. Pagliocca, K. Z. Uddin, I. A. Anni, C. Shen, G. Youssef, B. Koohbor, *Mater. Des.* **2022**, *215*, 110446.
- [53] Y. Chen, T. Li, F. Scarpa, L. Wang, *Phys. Rev. Appl.* **2017**, *7*, 024012.